Available online at www.sciencedirect.com
SCIENCE DIRECT®
Deep-Sea Research I 51 (2004) 1075–1096
DEEP-SEA RESEARCH PART I
www.elsevier.com/locate/dsr

Spatial structure of tidal and residual currents as observed over the shelf break in the Bay of Biscay

Frans-Peter A. Lam*[,1], Leo R.M. Maas, Theo Gerkema[2]

Royal Netherlands Institute for Sea Research (NIOZ), PO Box 59, 1790 AB Texel, The Netherlands

Received 23 December 2002; received in revised form 23 September 2003; accepted 5 March 2004

Abstract

Theoretical and laboratory models show that internal-wave energy in continuously stratified fluids propagates in the vertical plane, at an angle set by the wave, buoyancy and Coriolis frequencies. Repeated Acoustic Doppler Current Profiler observations on three transects, crossing the shelf edge, now directly reveal this beam-wise propagation of internal tides in the Bay of Biscay. This confirms previous suggestions based on observations sampled more sparsely in space. The present observation is made by bin-wise harmonic analysis of horizontal currents, leading to the spatial resolution of barotropic and baroclinic semi-diurnal tidal and (time-averaged) residual flows.

The observed barotropic tide has a cross-slope mass flux that is roughly constant. Its fast along-slope phase variations can only in part be explained by the spring-neap tidal cycle. The observed baroclinic tide compares favourably to that produced by a 2D numerical model. The observations reveal details of the internal tidal beam, including its spatial amplitude distribution, presence of amphidromes and direction of phase propagation. The cross-isobath structure of the along-slope barotropic mean flow shows a localized maximum near the shelf break. Over two transects it agrees in sign and magnitude with a theoretical tidally rectified flow. The baroclinic, cross-isobath mean flow shows a strong near-bottom downwelling flow, compensated by an on-shelf-directed flow in the upper part. The along-shelf mean flow displays subsurface intensification attributed here to frictional modification of a tidally rectified flow that is bottom-trapped due to stratification.

Keywords: ADCP observations; Tides; Internal tides; Tidal rectification; Internal tidal beams; Bay of Biscay; Internal waves; (Continental) shelf break

1. Introduction

In the oceanographic literature on internal waves in continuously stratified seas there has been an emphasis on their vertical modal structure. This approach entails two problems. Usually only a few modes are taken into account; thus a description of a narrow beam arising from a

*Corresponding author. Fax: +31-70-374-0654.
E-mail address: frans-peter.lam@tno.nl (F.-P.A. Lam).
[1]Present address. TNO Physics & Electronics Laboratory (TNO-FEL), Underwater Acoustics Department, PO Box 96864, 2509 JG The Hague, The Netherlands.
[2]Present address. Laboratoire des Ecoulements Géophysiques et Industriels (LEGI), BP 53, 38041 Grenoble Cedex, France.

0967-0637/$ - see front matter © 2004 Elsevier Ltd. All rights reserved.
doi:10.1016/j.dsr.2004.03.008

localized source (deWitt et al., 1986), with its typical phase and energy propagation, becomes impossible. A more fundamental problem occurs when the bottom is sloping, in which case internal wave propagation cannot be described by vertical modes (despite the fact that at each location a decomposition is possible). In a beam-like description of internal waves these problems are circumvented; it reveals the quite peculiar dispersion characteristics of these waves, which distinguish them from interfacial and surface waves. Internal waves in a continuously stratified fluid propagate obliquely, under some specific angle with gravity, defined by wave frequency ω and local buoyancy frequency $N(z)$, and when the fluid is rotating also by the Coriolis frequency $f < N$. Phase velocity is perpendicular to group velocity and they have opposing vertical components. The group velocity is in the direction in which energy propagates, and is parallel to the main axis of the alternating fluid motion. We expect the internal wave beam to be observable and test its oblique propagation on observations from the Bay of Biscay.

The peculiar dispersion characteristics of internal waves have been demonstrated lucidly in laboratory experiments (Görtler, 1943; Mowbray and Rarity, 1967; Dalziel et al., 1998; Sutherland et al., 1999, 2000). A tank in a laboratory is of course much simpler than the ocean: it is nonrotating, has uniform stratification, simple topography and no steady currents. However, we intend to show here, by again making use of relatively recent technology (i.e. a towed Acoustic Doppler Current Profiler—ADCP) that, despite these differences, one is able to recognize the beam-wise propagation of internal waves, alluded to above, also in the ocean: a 'tank' about a million times larger as the one for example shown in Sutherland et al. (1999, Fig. 3). Moreover, the measurements will provide us with estimates of the barotropic and tidally averaged barotropic and baroclinic fields in the vicinity of the shelf edge, which will be discussed separately.

The region of observation is a part of the Bay of Biscay, well-known for its strong internal tides. Baines (1982) estimates the northwest European shelf (taken roughly from Biscay to the Hebrides, west of Scotland) to be one of the highest contributors to the global internal tidal energy flux. Strong, localized internal tides (internal waves of tidal frequency) in the Bay of Biscay result from a combination of favourable stratification, steep topography and strong barotropic tidal currents directed cross-isobath (Cartwright et al., 1980; Baines, 1982; Le Cann, 1990). Away from the shelf edge, on the shelf and in the deep sea, these can give rise to internal solitary waves with thermocline depressions down to 50 m, especially in late summer (Pingree and Mardell, 1985). In Pingree et al. (1986) the internal tidal wave, travelling away from the shelf break in both directions, was explored with a well-designed observational program at sea. They found that the coastward travelling internal tide, if corrected for strong barotropic tidal advection, could be well explained by a so-called first mode (linear) description. Therefore, a two-layer description is adequate on the continental shelf for the phase propagation. For the oceanward travelling internal tide, a first mode did not suffice to describe the observed isotherm displacements and higher modes were needed to explain the observed spatial structure. In fact the third mode is dominant (Pingree and New, 1991).

Pingree and New (1989) found evidence for downward propagation of internal tidal energy into the ocean along characteristics. After a subsequent bottom reflection (Pingree and New, 1991), the beam forms even a second source of internal solitary waves, approximately 140 km away from the shelf edge, where it reaches the thermocline (New and Pingree, 1992; New and Da Silva, 2002). Ray and Mitchum (1997) suggest that the higher mode behaviour of the internal tide in the Bay of Biscay (and thus its beam-like nature) makes it more susceptible to changes in stratification, thus preventing the internal tide from being observed coherently at the surface with altimetry measurements. Therefore, in line with theoretical and laboratory findings (Maas and Lam, 1995; Maas et al., 1997), field observations too require a ray description of internal tides (Leont'yeva et al., 1992; Vlasenko and Morozov, 1993). Here, we present direct field observations in support of this ray or beam-like interpretation of the deep internal tide, in and near its generation area.

In laboratory experiments (e.g. Mowbray and Rarity, 1967), the forcing is simply an oscillating body. Near the shelf break the forcing is defined by vertical motion due to tidal flow over the continental slope. Also, unlike in any laboratory experiment, there is no 'camera' available to get the whole region into scope. Yet, by measuring with a towed ADCP one can obtain a quasi-synoptic image in a 2D (vertical) *xz*-plane of the barotropic and baroclinic structure of tidal and residual fields in the vicinity of the shelf edge.

In Section 2, we will discuss ADCP-sampling, the employed observational strategy. Emphasis in this study is on resolving the baroclinic tides and residual flow along and near the shelf break. Aiming to capture these, we sailed up and down a cross-slope track as fast as possible, sampling each of the three 13 km long, cross-slope tracks for some 10 times during two tidal cycles. Fitting a semi-diurnal tide to the 10 observations that we obtain for each bin in the (approximately 2D) vertical observational plane allows us to estimate tidal amplitude, phase and time-average (residual) of each current component, yielding a high spatial resolution of the barotropic and baroclinic tidal and residual fields.

In Section 3 the observed tidal data are presented, as well as some related simple theoretical and numerical models. Barotropic (depth-independent) tidal currents, Section 3.1, are discussed. We use the observed barotropic tide and stratification to evaluate the theoretical, internal-tide forcing term (as adopted in the model), which tells us how the forcing is distributed spatially. Baroclinic tides, Section 3.2, computed from this forcing, will be compared with those observed.

In Section 4 the offset of the estimated periodic motion in each bin is interpreted as the approximate stationary (residual) motion over the duration of the observation. Finding a reliable residual current is, however, more difficult than obtaining the tidal part: we are trying to extract a relatively small (time) mean from a signal that is dominated by the periodic motion, where the latter is itself complicated and subject to large errorbars. The resulting mean values might therefore be questionable, but, comparison with theoretical values match surprisingly well, and are within the right order of magnitude. Finally, in Section 5 the results are discussed and conclusions are drawn.

2. Sampling strategy

2.1. Towed ADCP measurements

Observations with a moving downward looking acoustic Doppler current profiler (ADCP), towed or ship-mounted, have been reported quite a lot in recent oceanographic literature. Spectacular improvements have been achieved in the quality of current measurements due to the use of differential global positioning systems (dGPS), on-line corrections for ship's motion (bottom tracking) and more available computer power (memory and storage capacities) in general. Subsequent data analysis is different from standard treatment of time-series (like, e.g. that of a moored current meter): the observations are *space–time series*. At this stage several different approaches are available to deal with measurements at different times and positions, and, more specifically, to split off tidal variability from lower frequency variability.

First, one can adjust the observational strategy to the (possibly dominating) tidal time and length scales. As a result, ship's tracks are repeated, so that every vertical bin of each interval of the track (horizontal bin) can be treated as a traditional mooring. In general, this delivers shorter time-series, but with a much higher spatial resolution. An impressive example of this method is given by Geyer and Signell (1990), who used a number of repeated tracks in an extensive campaign to produce maps of amplitude and phase for M_2, M_4, M_6 frequencies, as well as residual currents (eddies) for Vinyard Sound, near Cape Cod. Simpson et al. (1990) used a repeated track to estimate tidal amplitudes and phases, as well as residual throughflow in the channel between the outer Hebrides and the westcoast of Scotland (the Minch). Lwiza et al. (1991) used the same strategy to resolve the spatial structure of two cross-sections of a front in the North Sea. Two cruises of a repeated track, 1 week apart, could be combined to estimate amplitudes and phases for both M_2 and S_2 frequencies. In Simpson et al.

(1990) a fixed ratio between M_2 and S_2 amplitudes was presumed to obtain a spring-neap cycle. In general, the inability to resolve motion of M_2 and S_2 frequencies is a problem in the (mostly short) time-series of the mentioned repeated tracks.

Second, the horizontal structure of the tidal velocity field can also be obtained from arbitrary ship's tracks (Candela et al., 1992). By appealing to continuity, the vertical tide was inferred. The vertical structure in the measured (tidal) horizontal velocity field was, however, not discussed.

The data set described below is obtained by following the first strategy of repeated tracks, which allows determination of both the horizontal and vertical structure of the tidal and residual fields. The observations show that by repeating tracks several times within about two tidal cycles, sufficient information is gathered to obtain coherent information on the vertical structure of the tidal (and residual) field.

2.2. Sampling strategy in Bay of Biscay

From June 4 to June 8 1993 three transects over the shelf break in the Bay of Biscay were monitored for about 24 h each, as part of the *Triple B '93* project (van Aken, 2000). The transects 1, 2 and 3 (approximately in cross-isobath direction) had a length of about 13 km each, and were about 35 km apart along the shelf break (Fig. 1, Table 1). The ship was towing a downward looking narrowband (75 kHz, *RD Instruments*) ADCP, measuring the 3D current speed from 10 m below the water surface to the sea floor in 'bins' with thickness of 8 m. When the bottom is deeper than 800 m, the bottom could not be detected anymore, and correction for the ship's speed then had to be based on dGPS information, thereby deteriorating the measurement of the water velocity. While sailing up and down along transects 1, 2 and 3, the tracks were repeated 10, 14 and 11 times, respectively. Deviations from the track in the along-slope direction were small: well within 250 m most of the time. Any bin thus has at least 10 measurements of each of the velocity components in it. For the present purpose—the resolution of internal tidal and tidally rectified currents—bins are taken 250 m long, and measurements have been averaged within each bin. These are subsequently used to estimate the amplitude and phase of the semi-diurnal lunar (M_2) tide and the time-averaged (residual) flow in that bin. The remaining 7 degrees of freedom were used to improve statistical reliability of these estimates, and together determine the level of the 'unexplained' variance in the remainder of the signal.

Size and duration of the experiments were chosen in order to resolve, within the limits set by available ship time, ship's speed, etc., the tidal temporal scales near the shelf break as well as possible. But, we cannot also *spatially* resolve the large-scale barotropic tide in the observed quantities. From an observational point of view, it is not so easy to split barotropic and baroclinic motion in the measurements for three reasons. First, bottom friction leads to variations of the barotropic current in the vertical (Prandle, 1982; Maas and van Haren, 1987), significant especially in shallow water; second, ADCP measurements always lack reliable data from the top and bottom layers; finally, tidal advection of geostrophic fronts falsely suggest free internal tides (van Haren and Maas, 1987; Loder et al., 1992). However, for pragmatic reasons we will adopt standard practice and treat the vertical average as the barotropic, and the remainder as the baroclinic part. Note that all values with a depth deeper than 85% of the bottom depth have been disregarded in this vertical mean, because below that depth the acoustic beams of the ADCP are known to be suffering from interference with bottom reflected sidelobes.

2.3. Modelling the barotropic forcing of the baroclinic tide

The barotropic tide thus obtained will be used in the forcing term of an internal tide generation model, discussed in Section 3.2, which also needs a topography and stratification.

Small-scale structures in the topography (like canyons) lead to strong local variations in the barotropic tide. This leads to local variations in the strength of the internal-tide generating terms which is perhaps responsible for the surface

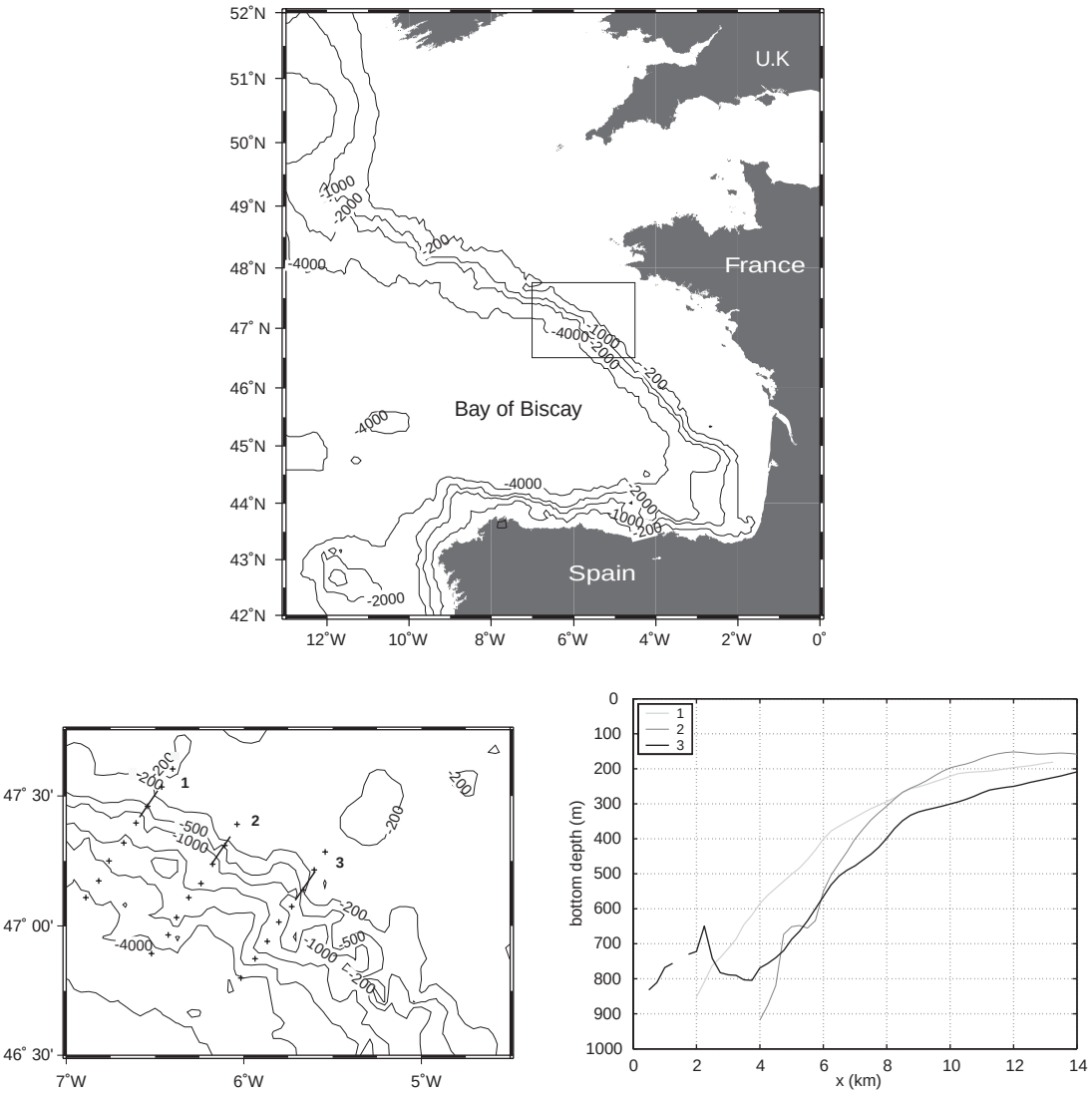

Fig. 1. Bay of Biscay bathymetry (top), with an enlargement of the sampling area (lower left) and the ADCP-measured bottom depth for the 3 transects (lower right). In the lower left panel, towed ADCP-transects 1, 2 and 3 are depicted from left to right (straight solid lines). CTD-stations are marked with +. The bathymetry is from the ETOPO-5, 5-min database (large area), and the enlargement with improved 2-min NOAA database (Smith and Sandwell, 1997). The position of each local origin (most south-western point of each transect) and the orientation of the *x*-axis in the lower right panel and all subsequent figures is given in Table 1. As a reference in the enlargement, note that the distance between two tick labels (30 min) in the north-southward direction corresponds to 30 nautical miles, or approximately 56 km.

impression of radially diverging internal tides, seen on satellite (SAR) pictures (New, 1988, Fig. 3). This may also explain strong spatial variations in observations of currents (Holt and Thorpe, 1997). These 3D features can unfortunately not be captured in the present approach.

An approximate density profile for the region under study, as presented in the next section, is obtained with the CTD-casts from the simultaneous hydrographic program. e.g. (van Aken, 2000). Along each transect, eight CTD-stations were located oceanward and across the shelf

break, as depicted in Fig. 1. We will idealize these aspects in the internal tide generation model by neglecting depth variations along the shelf, and by calculating a forcing term from an ensemble average stratification and a typical cross-isobath bathymetry.

3. Tidal currents: observations and model results

3.1. Barotropic tide

An example of the method of estimating barotropic tidal amplitudes from repeated tracks is given in Fig. 2, where we display the barotropic current velocities (open circles) as determined and approximated by depth averaging. The currents, u and v, are in cross-slope (x) and along-slope (y) directions, respectively (see Table 1). For each of the transects, the most south-westward point visited was taken as the local origin of this coordinate frame. The position at $x = 10$ km on transect 1 shown here is passed 10 times, and the least-squares fit to M_2-periodicity (frequency ω) gives amplitudes of 58 and 31 cm/s for cross-slope and along-slope velocity components, respectively. The velocity components are approximately 90 degrees out of phase, with v leading u, implying anticyclonic (clockwise, for $f > 0$) polarized motion, and the offset supplies an estimate of the residual currents, which we will deal with later on. We obtain these figures by assuming that at each position the velocity components can be written (e.g. for the cross-slope component) as

$$u = U_0 + U_2 \cos(\omega t + \phi_u) + u_\varepsilon(t). \quad (1)$$

Here ϕ_u, U_0 and U_2 are constants, defining tidal phase, and the residual and tidal velocity amplitudes, respectively. These are determined by a least-squares fit of this model to the data, which minimizes the error $u_\varepsilon(t)$. Here $t = 0$ is defined as 00:00 UTC, January 1, 1993.

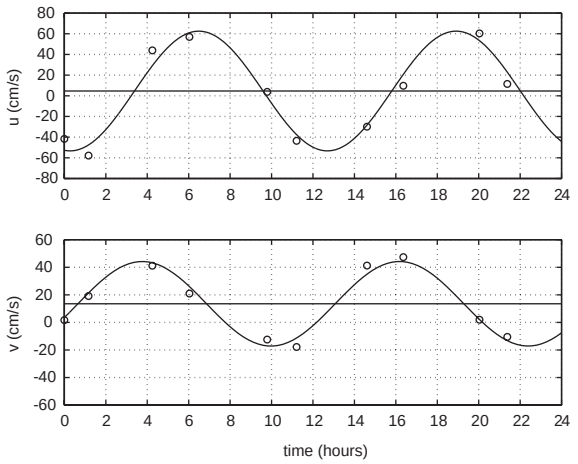

Fig. 2. Example of a fit to the bin-wise observed velocity data in cross-slope (u) and along-slope (v) direction. In this example, time is measured in hours from the first crossing. The observations are marked with circles (o) and are fitted by a cosine and an offset (horizontal lines).

Table 1
Positions, orientation, dates and duration of ADCP-transects

Transect	1	2	3
Latitude	47.4186°N	47.2356°N	47.1010°N
Longitude	6.5881°W	6.1814°W	5.7106°W
α (True North)	34.2°	32.7°	34.7°
Start date 1993	June 4	June 6	June 8
Duration (h)	22.7	27.6	25.7
# Repeated tracks	10	14	11

Positions correspond to the most southward visited point, and is defined in all following figures as $x = 0$.

A spatial overview of the observed features of the barotropic semi-diurnal tides along the three transects is given in Fig. 3. We find high cross-slope velocities, up to 80 cm/s, which are about twice as large as the along-slope velocities. The amplitudes are roughly inversely proportional with depth (see the lower panels depicting mass transports uh and vh), so the cross-isobath flux is approximately constant (to within 30%), especially for $x > 7$ km. Transect 1 was measured near spring tides, while transect 3, taken approximately 3.5 days later, was closer to neap tides. Because we could not resolve separate tidal constituents, like M_2 and S_2, it is hard to compare these values with values of M_2 from harmonic analysis of other observations of longer duration. Nearby, at a waterdepth of 310 m, Pérenne (1997) resolved several tidal components (M_2, N_2, S_2 and K_2) with a bottom-moored ADCP which together lead to transports of comparable magnitude. Also the

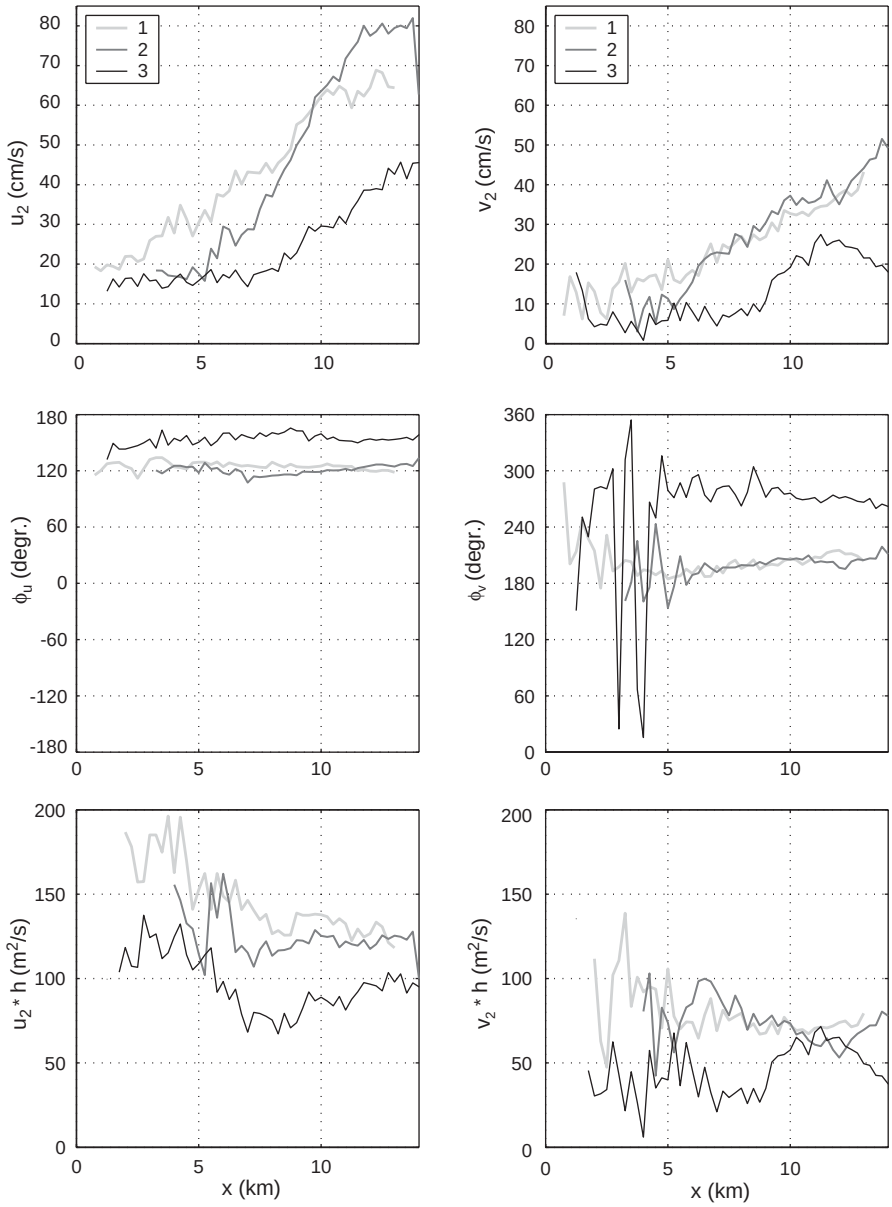

Fig. 3. Observed barotropic velocity and transport. Cross-slope (left) and along-slope (right) velocity amplitudes (top), phase (middle) and transport (bottom). Transect 1, 2 and 3 are depicted as indicated in the legends in the top frames. The topography used is the same as shown in Fig. 1.

ellipticities are comparable: the cross-slope amplitudes are roughly twice as large as the along-slope amplitudes and the circulation is anti-cyclonic or clock-wise.

Phases of the velocity components (middle-left and middle-right panels of Fig. 3) are fairly constant over cross-slope distance x, but they differ quite a lot in magnitude: differences of about 50° for cross-slope phase (ϕ_u) and 70° for along-slope phase (ϕ_v) can be seen between subsequent transects. These differences are much too large to be explained by a monochromatic, barotropic

deep-sea Kelvin wave, with phase speed $c = \sqrt{gh} \approx 200$ m/s, which, for the semi-diurnal tide, has a wavelength of about 9000 km. The transects are only about 35 km apart in the along-slope direction, so this would give an approximate phase difference of about 2.8°. If the deep-sea Kelvin wave is somewhat 'delayed' by the presence of the shallow shelf edge, its phase speed (wavelength) will be a little less (shorter), but for the actual situation differs always less than 10% (Miles, 1972). It can be shown (by using the same method as in Simpson et al., 1990) that inclusion of the S_2 component can explain additional differences (in the combined or mixed signal) of up to 15–20°, with perhaps additional phase differences due to other tidal components. But, this will not be sufficient to explain the observed large phase difference. More observations are needed to resolve this aspect.

3.2. Internal tide

3.2.1. Forcing

As already mentioned in Section 2, in the forcing of internal tides three elements are essential: topography, a (cross-slope) barotropic tidal flow, and stratification. In estimating the strength of the forcing, we shall assume (as is usual, see e.g. Baines, 1973) that the cross-slope barotropic tidal flux is constant in space. In reality, the amplitude of the cross-slope barotropic flux will decrease oceanward on the scale of the (barotropic) Rossby radius of deformation, as well as coastward on the scale of the shelf width (see, e.g., the discussion in Le Cann, 1990, Section 4.3); however, since both scales are large compared to the width of the shelf break region, where the main generation of internal tides takes place, the assumption of a constant flux can be considered justifiable. This is corroborated by the observations described in the previous subsection.

The forcing F is thus constructed by prescribing a cross-isobath barotropic tidal flow $U_2(t,x) = Q \sin \omega t / h(x)$; here Q is the amplitude of the barotropic flux, ω the tidal frequency, h the local depth, and x the cross-slope direction. Continuity requires that the vertical barotropic component be

$$W = zQ \sin \omega t (\mathrm{d}h/\mathrm{d}x)/h^2, \tag{2}$$

where the boundary condition $W = 0$ at $z = 0$ (upper surface, rigid lid) is satisfied. Hence the forcing term to be included in the buoyancy equation becomes

$$F = N^2 W = zN^2 \frac{Q \sin \omega t}{h^2} \frac{\mathrm{d}h}{\mathrm{d}x} \equiv \hat{F} Q \sin \omega t. \tag{3}$$

The spatially depending factor $\hat{F}$ is depicted in Fig. 5a and depends only on topography and stratification. The latter requires the spatial distribution of potential density to be known. The complete forcing term F differs slightly from the forcing term in Baines (1982), which was included in the momentum equations instead; for the end results this makes no difference.

Preceding the repeated tracks of every ADCP-transect, 8 CTD-stations were visited along the same tracks, extending further into the deep sea. Unfortunately, as is clear from Fig. 1, only a few of the CTD-stations lie on transects sampled with the towed ADCP afterwards. It is known that a banded structure, or shelf break front, exists along the 200 m isobath approximately, see e.g. Serpette and Mazé (1989) and Pingree and New (1995, their Fig. 10); with the given measurements, this structure is not adequately resolved. Moreover, the CTD-observations are snapshots of the density profile in an expectedly energetic internal tide/wave field. For example, in a nearby observation at a 'deeper extension' of transect 2, not shown here, over a water depth of approximately 1300 m, CTD-yoyoing revealed the presence of isothermal elevations of the order of 300 m on time-scales from 1 h to the tidal period (van Aken, pers. comm.). Ideally, each position should have been sampled for several tidal periods. Since this was not done, we have to estimate the mean density field by appropriate averaging.

All in all, the density field $\rho(x,z,t)$ is not known in much detail with the given measurements, and hence neither is the buoyancy frequency N. To obtain the average stratification, $N(z)$, the 24 CTD casts were ensemble averaged and subsequently smoothed in the vertical by applying a running mean over distances of 101 m (Fig. 4, left panel).

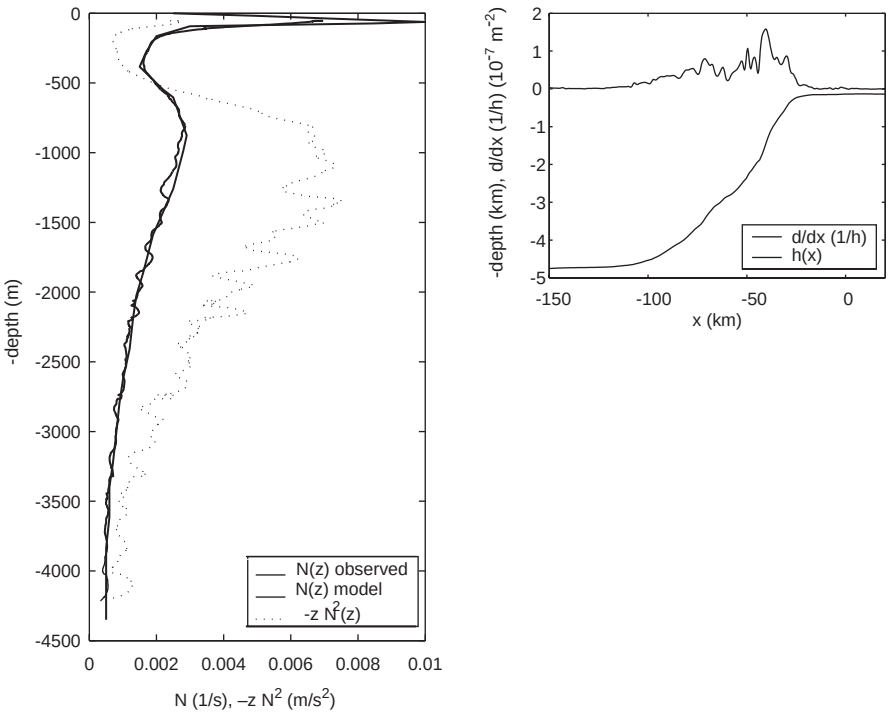

Fig. 4. Left panel: averaged Brunt-Väisälä frequency profile $N(z)$, smoothed over 100 m (full line) and $-zN^2(z)$ profiles (dotted line) in s^{-1} and m/s^2, respectively. All 24 different CTD-stations (see Fig. 1) are horizontally averaged. The smoother line is the profile used for the linear model calculations, see Section 3.2.1. The right panel contains information about the depth profile used for the linear model calculation (based on the depth profile corresponding to that of transect 2, see Fig. 1). Also depicted in the right panel is the effect of the topography, $\mathrm{d}/\mathrm{d}x(1/h)$ (units: $10^{-7}/m^2$).

In the model below this is again approximated (smooth line), retaining the sharp seasonal thermocline and deeper permanent thermocline typically found in this area (Pingree and New, 1991). This figure also displays $-zN^2(z)$ (dotted line), which represents the vertical dependence of the forcing term, (3). It is seen that, although $N(z)$ itself is much larger in the seasonal thermocline, the deeper regions (especially in and around the permanent pycnocline) can be expected to be of importance in the generation of internal tides. Furthermore, high variability in the estimate of $N(z)$ is clearly visible, despite the vertical smoothing used.

For the calculation of the horizontally varying part of the forcing (3), we used the topography observed on a transect traversed in a 1995 cruise. This transect was identical to transect 2, but extended farther coastward from the break. Fig. 4 (right panel) displays $\mathrm{d}(1/h)/\mathrm{d}x$. The buoyancy frequency N is taken as in Fig. 4 (left panel, smooth line), which is regarded as an average stratification. The spatial part of the internal-tide forcing (multiplied by a factor 10^9) is shown in Fig. 5a. The figure clearly shows that there are *two* main generation areas: one in or close to the seasonal thermocline, near the shelf break, the other at deeper positions in the permanent thermocline. Compared to Fig. 4, the seasonal thermocline has gained in relative importance thanks to its being present over shallower depths. It should be mentioned that the estimated body force given here involves some uncertainties in view of the only partly known density field as well as possible 3D-effects.

Though not as strong as in our observations, a second, deeper generation region was also found by Sherwin and Taylor (1990) further north in the

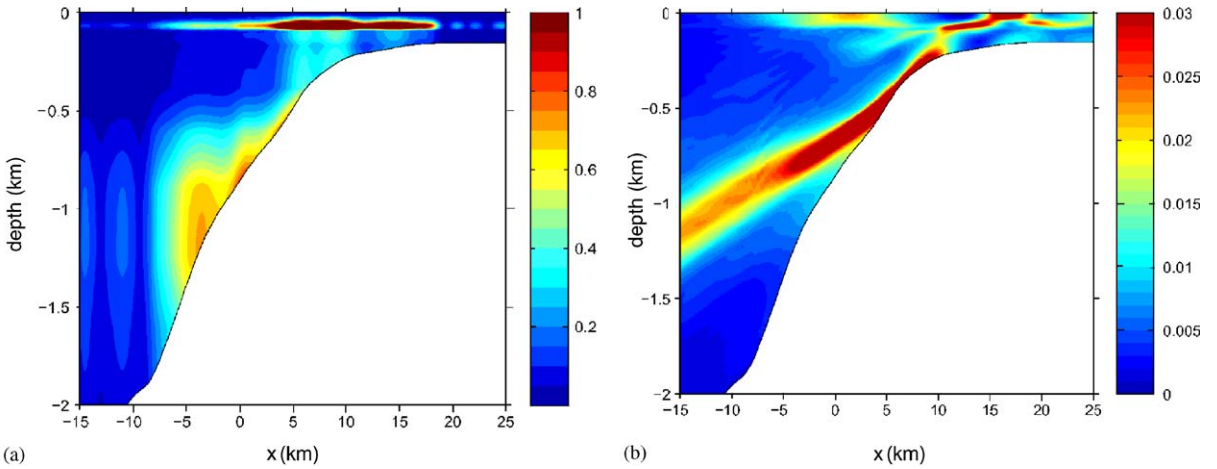

Fig. 5. (a) Spatial structure of forcing term $\hat{F}$ ($1/ms^2$) multiplied by 10^9, as defined by (3). (b) Same figure, but for internal tidal energy (m^2/s^2), as defined in (8). Units on the axes are in kilometers.

Rockall Trough, northwest of Ireland. In Fig. 5a we find a maximum value in the forcing in the thermocline that is about 2.5 times higher than that in Sherwin and Taylor (1990) (who present $\hat{F}\rho Q/\omega$ in their Fig. 4). This is due to a combination of a larger cross-shelf mass transport, steeper topography and possibly stronger stratification locally. In the deep generation area the forcing can be up to 10 times as big. If N were constant, such as one often assumes in (semi-) analytical models (e.g. in Baines, 1982), only a single, near-bottom generation region exists. Furthermore, due to the smooth topography, the generation regions are much more blurred in Fig. 5a than in for example Baines (1982), where (due to the piecewise linear topography) point-sources occur, giving rise to singularities in the velocity field (Gerkema, 2001, Appendix A).

3.2.2. Linear model results

The observed spatial structure of amplitude and phase (to be presented in the next subsection) can be compared with the outcome of a linear, hydrostatic internal-tide generation model (including Coriolis effects), which was previously described and used in Gerkema (2002). Here along-slope uniformity is assumed (i.e. $\partial/\partial y = 0$); we can therefore introduce a stream function ψ (expressing the baroclinic current speeds as $u = \psi_z$ and $w = -\psi_x$), and reduce the linear long-wave equations to

$$\psi_{zzt} - fv_z - \rho_x = 0, \tag{4}$$

$$v_t + f\psi_z = 0, \tag{5}$$

$$\rho_t + N^2\psi_x = N^2 W = F \tag{6}$$

in which f is the Coriolis parameter, v transverse velocity component, and ρ the potential-density perturbation with respect to its local static value (multiplied by g/ρ_*, for convenience, where g is the acceleration due to gravity, and ρ_* the mean density). F, given by (3), represents the forcing due to the barotropic tidal flow over the topography.

Before we turn to the forced problem, it is useful (in view of the considerations put forward below) to recapitulate first some known theoretical results concerning internal-wave propagation, which follow from the unforced version ($F = 0$) of the model Eqs. (4)–(6) if we assume that N is nearly constant. One finds, by assuming that all fields can be written as a constant times $\exp(i(kx + mz - \omega t))$, the dispersion relation

$$\omega^2 = N^2 \cot^2\theta + f^2, \tag{7}$$

where $\tan\theta \equiv m/k = \sqrt{N^2/(\omega^2 - f^2)}$. The dispersion relation depends only on the direction of the wavevector $\vec{k} = (k, m)$, which implies that the

group-velocity vector $\vec{c}_g$ must be perpendicular to it: $\vec{k} \perp \vec{c}_g \parallel \vec{u}$ (the latter follows from the continuity equation, $\nabla \cdot \vec{u} = 0$). Hence the wave-energy propagates along lines of equal phase, being given by $dx/dz = \tan\theta$. Furthermore, $\vec{c}_g$, being a gradient in wavenumber–space, points (by definition) in the direction of increasing ω; in this case $f < \omega \ll N$, which implies that the vertical components of $\vec{k}$ and $\vec{c}_g$ must be opposite. Hence, where phase-propagation is upward, energy propagates downward (and vice versa). In the next subsection we shall check these results against the observations.

The input values for the topography and stratification are as described in the previous subsection. Based on Fig. 3, the barotropic cross-slope flux is taken to be $Q = 100\ \mathrm{m}^2/\mathrm{s}$, corresponding with current speeds of about 2 cm/s in the deep ocean—being comparable to values found by Pingree and New (1991, their Table 1). Notice that the value of Q is immaterial to the *structure* of the solution since the equations are linear.

As discussed in Gerkema (2002), the equations are solved by first transforming the xz-domain to a rectangular shape, which allows the application of a pseudo-spectral method in the vertical, involving here 64 Chebyshev polynomials. The boundary condition is $\psi = 0$ at bottom and surface. In the horizontal and in time centered differences are used (steps of 400 m in x, 360 time steps per tidal period). At the outer ends of the domain sponge layers are used to absorb the incoming waves. The fluid is initially at rest; after about 40 tidal periods the transients have left the region of interest, and the signal has become periodic in time.

The tidally averaged energy density $\langle E \rangle$, E being here defined as

$$E = \tfrac{1}{2}(u^2 + v^2 + \rho^2/N^2), \tag{8}$$

is shown in Fig. 5b. Surprisingly perhaps, in its details there is no strong similarity with the forcing term (shown in Fig. 5a); in particular, the main beam emanates from the topography (shelf break) rather than from the thermocline, despite the fact that the actual forcing term is stronger in the latter. This is because the generation is most efficient on those locations where the barotropic pair of components (U, W) is (literally) in line with the baroclinic tidal components (u, w), the direction of which is fixed by the stratification and Coriolis parameter; see (7). This condition is satisfied precisely at critical locations at the slope, i.e. where the steepness of the beam equals that of the slope.

On the whole, one can discern three regions in Fig. 5b of internal tide activity: a clear beam directed downward into the deep ocean, a weaker beam directed on-shelf, and a relatively high-energy region near the surface at the deep side of the shelf break (near $x = 0$). This region starts in the thermocline and does not emanate as a beam from the shelf break; such a beam is predicted for piecewise linear topography (point source, see Baines, 1982; New, 1988), but is absent here because of smooth topography. As the on-shelf propagating beam and the strong near-surface currents at the deep side of the break emanate from the seasonal thermocline, one may expect that they will be absent during winter. Further numerical results confirm this (Gerkema et al. in press): during winter only the downward–oceanward beam is present. In Gerkema et al., (in press) the seasonal differences in the overall energetics of the internal tide is discussed as well.

The cross-slope baroclinic component u can be written as

$$u(t, x, z) = A(x, z)\sin(\omega t + \phi(x, z)). \tag{9}$$

The spatial structure of amplitude A and phase ϕ is shown in Fig. 6; (9) implies that the lines of equal phase propagate in the direction of decreasing ϕ. Thus Fig. 6b divides almost perfectly into two parts, the division lying near $x \approx 6$ km: to its right phases propagate downward (except in the lower right corner), to its left upward. The latter does not hold in the region near the surface around $x = 5$ km, where phases propagate downward. Notice that this region coincides with that of the beam directed up—and oceanward in Fig. 5b.

A striking feature connected with this is what we may call an 'amphidromic' point, which lies near $x = 6$ km, just below 200 m depth. Unlike the common amphidromes occurring in barotropic tides, this one appears in the *vertical* plane; such an amphidrome was previously found in numerical (deWitt et al., 1986) and analytical (Gerkema, 2001) internal-tide solutions, but not, to our

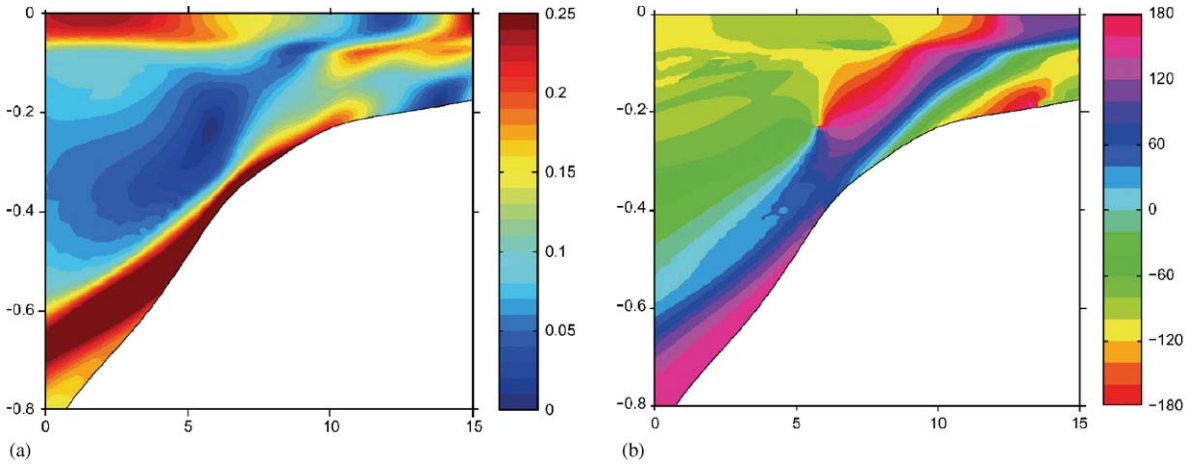

Fig. 6. Linear model results of cross-slope baroclinic motion. Left panel (a) depicts amplitude distribution (m/s). Right panel (b) shows phases in degrees. Units on the axes are in kilometers.

knowledge, in real observations (but see next subsection). Also remarkable is the diagonal band (blue) in which the amplitudes are very small. In the next subsection Fig. 6 will be compared with the observed data.

3.2.3. *Observed internal tide*

In Section 3.1 the barotropic tide was assumed to be represented by the vertical mean of the estimated tidal motion, and so the internal (baroclinic) tide will consequently be assumed to be that part of the tidal motion that deviates from this vertical mean. The internal-tidal current thus defined is represented in terms of amplitude and phase distributions as indicated in (1). The observed patterns of tidal amplitudes (u_2, v_2) and phases (ϕ_u, ϕ_v) are shown in Figs. 7 and 8. Qualitatively, one can distinguish three regions where strong currents occur: close to the slope, in the upper left-half, and in the upper right corner; they are separated by (blue) diagonal bands. This (rough) qualitative picture corresponds very well with the numerical results in Fig. 6a. Phase propagation is generally upward (i.e. in the direction of decreasing ϕ, see previous subsection) in the left-half of each figure, and (though less clearly) downward in the outer right part. Again, this is in qualitative agreement with the numerical result shown in Fig. 6b. Indeed one can discern the earlier mentioned amphidromes: for transect 1 near $x = 4.5$ km at 270 m depth; for transect 2 near $x = 7$ km at 250 m depth; for transect 3 near $x = 6.5$ km at 290 m depth.

Overall, one sees distinct diagonal bands of equal phase in Fig. 8, in qualitative agreement with results on internal-wave propagation established previously in laboratory experiments (e.g. Mowbray and Rarity, 1967; Sutherland et al., 2000), oceanic observations on internal tides (deWitt et al., 1986; Pingree and New, 1989; Morozov, 1995) and theory (LeBlond and Mysak, 1978). Exact comparison with linear internal-wave theory is straightforward. First of all, phase- and energy propagation should have opposite vertical components (see previous subsection); this means that, both in Figs. 6b and in 8, energy propagates generally down- and leftwards in the left-half of each figure, and up- and rightwards in the (outer) right-half; in other words, energy propagates away from the source (the shelf break), as one would indeed expect. Eq. (5) implies that u and v should be out of phase by 90° if no along-slope variations were present; this seems indeed to be the case for all transects, as can be seen in Fig. 9, especially in those regions where the beam is intense.

Finally, we consider the slope of the lines of equal phase. The observed (inverted) slope (see Figs. 7 and 8) is about 5 km/250 m, in agreement with that obtained from the numerical model (Fig. 6). This slope is for plane waves given by

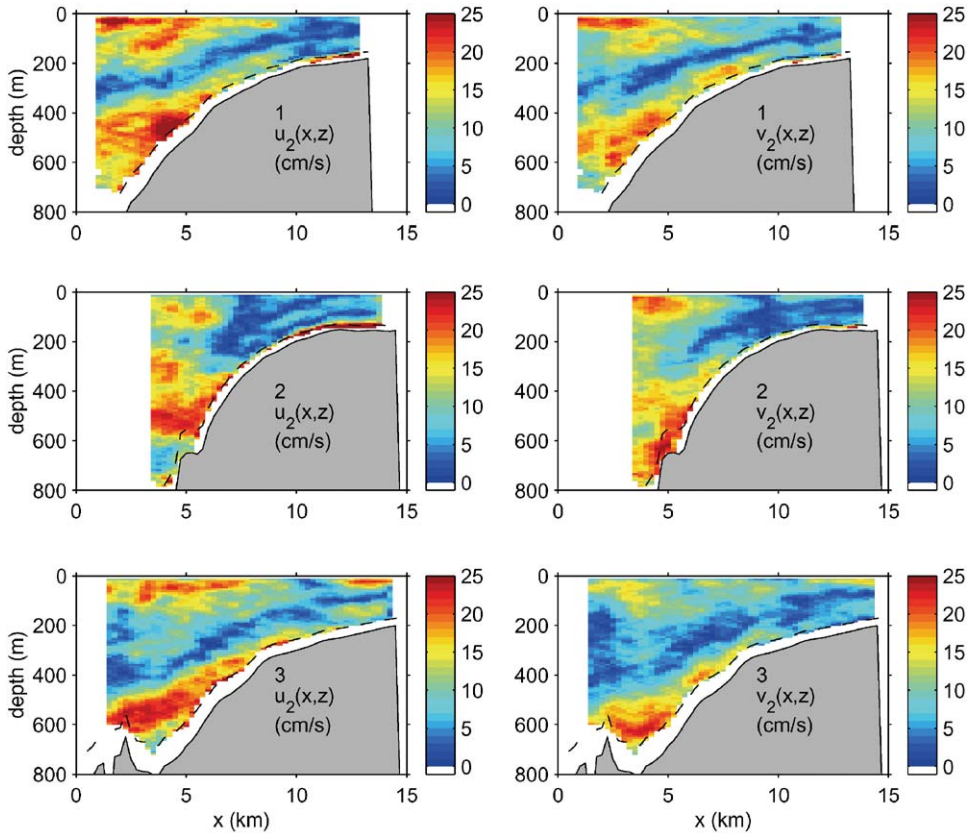

Fig. 7. Internal tidal amplitudes (in cm/s), in cross-slope (left) and along-slope (right) direction at transects 1 (top), 2 (middle) and 3 (bottom). Dashed lines depicts 85% of the water depth. Measurements below these lines should be disregarded, as explained in Section 2.2.

$dx/dz = \tan\theta$, (7), which yields the same slope taking $N = 2.0 \times 10^{-3}$, and $f = 1.0 \times 10^{-4}$ and $\omega = 1.4 \times 10^{-4}$ (all in units: s^{-1}).

4. Residual currents: theory and observations

4.1. Possible driving mechanisms of slope currents

The slope current, in the Northern Hemisphere having the shelf at its right when facing downstream, is an ubiquitous phenomenon along shelf edges. Clockwise mean-flows are (in the Northern Hemisphere) often found around isolated seamounts too (Eriksen, 1991; Kunze and Toole, 1997). The slope current is attributed to a number of causes, discussed in Pingree and Le Cann (1989, 1990) and Huthnance (1984, 1992). These include wind, a large-scale, along-shelf poleward density gradient, a shelf-slope frontal system (of which the slope current is the associated, geostrophic flow), rectification of continental shelf waves, tidal waves (Zimmerman, 1978; Ou, 1999), and internal waves (Thorpe, 1999), or to a statistically forced flow (Kazantsev et al., 1998). Seasonality of current shear (weak in winter, strong in late summer) might reflect the geostrophic character of the flow, although Pingree and Le Cann (1990) estimate this geostrophic flow to be small for the present observation site (<1 cm/s). Persistence of the mean flow and modulation at the spring-neap tidal time-scale, are often, particularly in shallower water, interpreted as pointing at a tidal origin of the flow (Butman et al., 1982).

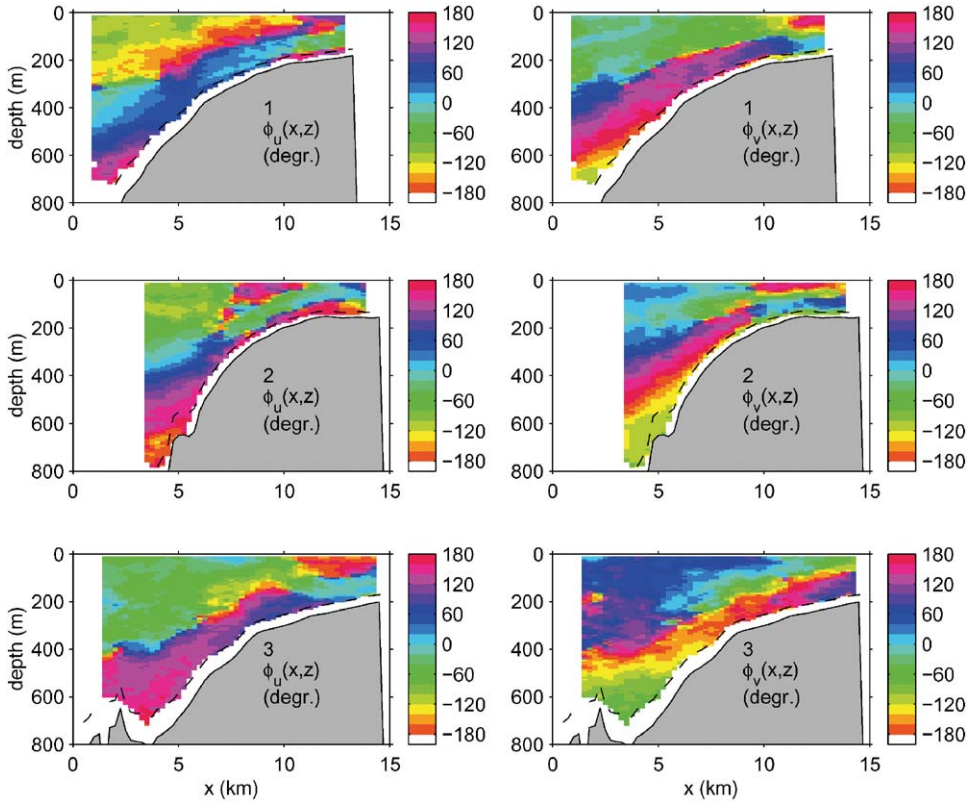

Fig. 8. Internal tidal phases (in degrees) corresponding to Fig. 7, i.e. deviations from vertical mean. Dashed lines represent 85% of the waterdepth, as in Fig. 7.

Although tidal rectification may be important near Chapel Bank, where tides are particularly strong (about 70–80 cm/s, Pingree and Le Cann, 1989), this process is generally not seen as a significant contributor to the slope current over the shelf break, owing to the large depths (> 200 m). Huthnance (1992), discussing the observed spring-neap tide modulation of the slope current, advances another argument, by noting that the phase of this modulation *lags* that of the tidal fortnightly modulation, which is taken as signalling a modulation in the amount of friction of the barotropic tide, rather than as a clear indication of tidal rectification. Tidal rectification is therefore usually considered important in shallower areas, on continental shelves (with their increased tidal currents), like over Georges Bank (Butman et al., 1982), or the North Sea (Huthnance, 1973; Zimmerman, 1978; Howarth and Huthnance, 1984). However, stratification may amplify the vortex stretching mechanism underlying the rectification process in deeper water too, by inhibiting vertical motions further away from the bottom, which may lead to a bottom-intensified, rectified flow (Maas and Zimmerman, 1989b; Chen and Beardsley, 1995). This is one of the reasons why tidal rectification may become important at and around seamounts, at several hundred meters depth (Eriksen, 1991).

4.2. Cross-slope circulation

The along-isobath slope current is often accompanied by cross-isobath currents. Near the bottom these are downslope at the upper, and upslope at the deeper stretches of the slope. Several hypotheses have been formulated to explain the cross-slope circulation. It might be a secondary circula-

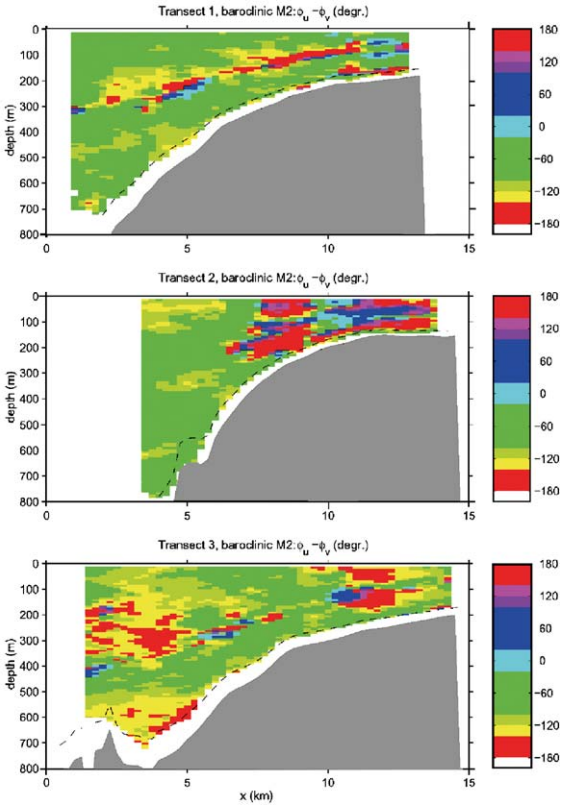

Fig. 9. Phase differences, $\phi_u - \phi_v$, as derived from Fig. 8. Dashed lines represent 85% of the waterdepth, as in Fig. 7.

tion of a rectified current system, whether of a frictional (Tee, 1985; Wright and Loder, 1985; Loder and Wright, 1985) or stratified origin (Ou and Maas, 1986; Maas and Zimmerman, 1989a,b; Chen and Beardsley, 1995). It might also result as a secondary circulation of a frontal system (Garrett and Loder, 1981), itself linked to the tide by tidal mixing. Indeed, the strongly nonlinear character of the external and internal tide, implying the presence of rectified flows and solitary waves, suggests that mixing may be particularly relevant in these areas too, which is indeed manifest in the consistent presence of a band of lower temperatures around the shelf edge, the 'cold ribbon'. This is a band (of width ~ 50 km) of relatively ($\sim 2^\circ$) cooler surface temperatures along the shelf break of the Bay of Biscay, seen on numerous satellite infra-red images of the region (e.g. Pingree, 1979; Pingree, 1984). Thus, strong tidal mixing will contribute to the shaping of (and be affected by) the shelf edge density front.

However, to settle which mechanism(s) is (are) responsible for the mean flow, it might be useful to find other observables that can distinguish between some of the proposed mechanisms. Contrasting the slope current as driven by a poleward buoyancy gradient with, for instance, a tidally rectified current, one might employ a predicted difference in cross-isobath structure of the residual flow to discriminate between the two. The along-slope, depth-mean flow

$$v = \frac{gH}{2r\bar{\rho}}\frac{\mathrm{d}\rho}{\mathrm{d}y}h(1-h/H) \tag{10}$$

(with H the depth of the adjacent deep sea) is expected to extend over the whole sloping region (Huthnance, 1984). This mean flow takes on its maximum approximately halfway over the slope (if we assume that on the shelf $h \ll H$). The tidally rectified current should be mainly concentrated over the top of the slope (Zhang et al., 1996):

$$v = -\frac{1}{2}\frac{fU^2H^2}{\omega^2h^3}\frac{\mathrm{d}h}{\mathrm{d}x}. \tag{11}$$

Here $\bar{\rho}$ and $\rho(y)$ denote the spatially constant and poleward y-varying part of the density field, f and ω the Coriolis and tidal frequency, U the tidal current speed on the shelf. Linearized friction is adopted in the former description, taking a velocity scale $r = 0.5$ cm/s. Note that this friction velocity is often parameterized as $r = C_D U$, where drag coefficient $C_D \approx 2.5 \times 10^{-3}$. Because cross-slope barotropic mass transport is nearly constant, an increase in depth leads to a decrease of U. The related decrease in friction velocity leads to a rapid increase of the slope current (10). Blaas et al. (2000), using a 2D numerical model, identify regions along the North Western European shelf edge where either one of these processes dominates, and regions where the slope current is actually a (nonlinear) superposition of residual currents due to both processes. They note that when the density gradient were restricted to the upper part of the water column, rather than the whole column, then the position of maximum flow in (10) would shift from halfway the slope towards the shelf, and weaken (Blaas et al., 2000; Blaas,

2002); however, we shall use (10) further on. In the following we will make such a comparison on the basis of the observed mean flow over the three transects.

4.3. Observed mean flow

The harmonic analysis of the towed ADCP-data offers us, apart from tidal information, also a binwise estimate along each transect of the 'residual' current as, e.g. in Loder et al. (1992).

Due to the shortness of our 'space–time' series, aliasing may disturb the individually estimated residual currents. This is a greater source of noise for the mean flow than for the tidal field because of the relative weakness of the former. As this may lead to very erratic spatial patterns, we interpret any spatial coherence in the residual current patterns as indicative of a well-determined residual field, although we recognize that the 'residual' may, in this case, contain also other low-frequency contributions, notably of a diurnal origin.

Rather than decomposing the mean flow into a (vertically averaged) barotropic and a (remaining) baroclinic part, it turns out to be more useful to consider only the barotropic and *total* mean flow patterns. Over the length of the transects this will provide a detailed picture of the spatial structure of the residual current, which will be compared with the theoretically predicted shape.

4.4. Observed barotropic currents

On transects 1 and 3 (Fig. 10) the vertically averaged, along-isobath residual current has a localized, jet-like structure, with a maximum amplitude of some 10–15 cm/s. The jet is centered near the shelf edge, over bottom depths of 200–300 m. Transect 2 has a somewhat similar structure, although the mean flow seems to extend to deeper water (peaks at $x = 3$ and 4 km). It may well be that these peaks result from the passage of what seems like a solitary wave, encountered during one of the ten traverses. Solitary waves are, after all, not uncommon in this area (Pingree and Mardell, 1985; Pingree et al., 1986; New, 1988; Pichon and Mazé, 1990).

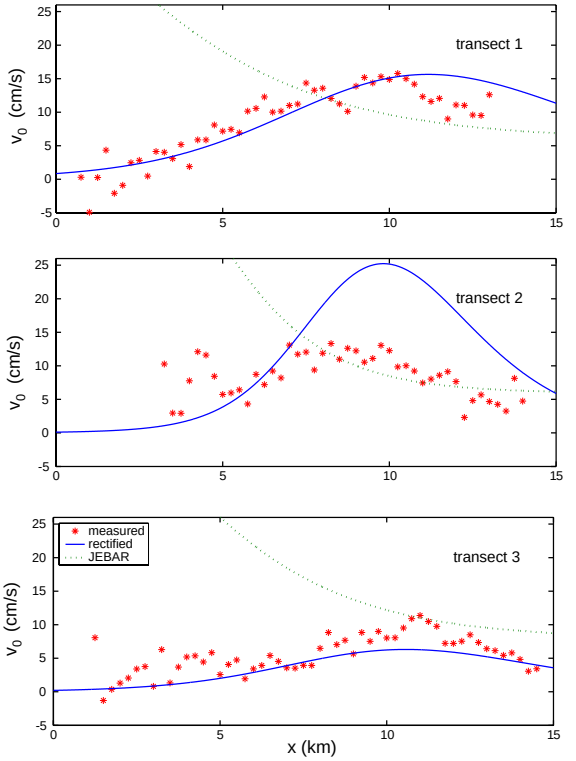

Fig. 10. Observed vertically averaged along-slope currents as a function of cross-slope distance x. Observed values (for each bin) are given by stars (*). Calculated rectification, as given by (11), is given by smooth lines. Here the observed topography is fitted to a tanh-shape. Calculated slope current, as given by (10) (JEBAR), is represented by dotted lines. Here the following values have been used: $r = 0.005$ m/s and $1/\bar{\rho}\,\partial\rho/\partial y = 10^{-10}$, the latter according to Blaas (2002).

The mean flow jet is some 8 km wide, and is, over the shallower regions, accompanied by vertically averaged on– and off–shelf flows of some 5 cm/s (not shown). The latter cross-isobath residual flows perhaps suggest an error in the local choice of cross and along-isobath direction, which may be more influenced by local bathymetric features, instead of by the large-scale shape of the shelf edge on which our present choice was based. The extent to which local canyons and shelf edge crevices influence the actual barotropic–baroclinic conversion process and the resulting mean flows, is currently a topic of research (Grimshaw et al., 1985; Holt and Thorpe, 1997; Petruncio et al., 1998).

Fig. 10 also contains theoretical profiles, determined by (11) (solid) and (10) (dotted). Except for transect 2, both the magnitude and the shape of the residual current seem well described by the barotropic, tidally rectified current of (11). Since the slope stretches out over some 60 km, the slope current due to the joint effect of baroclinicity and relief (JEBAR, Huthnance, 1984), given by (10), should, over the length of the transect, only increase in magnitude away from the shelf edge (dotted line in Fig. 10; the calculated maximum of the slope current being almost 50 cm/s).

4.5. Observed total currents

The bin-wise observed total residual currents are depicted in Fig. 11. The most remarkable features are a clear subsurface, along-isobath jet (red regions in right panels; recalling the comments with regards to the deeper parts of transect 2, made earlier) and the strong near-bottom, downslope cross-isobath currents (magnitudes of about 10–15 cm/s), over the shelf break region (blue regions in left panels).

The along-isobath current increases from the bottom upwards, reaching a maximum in the

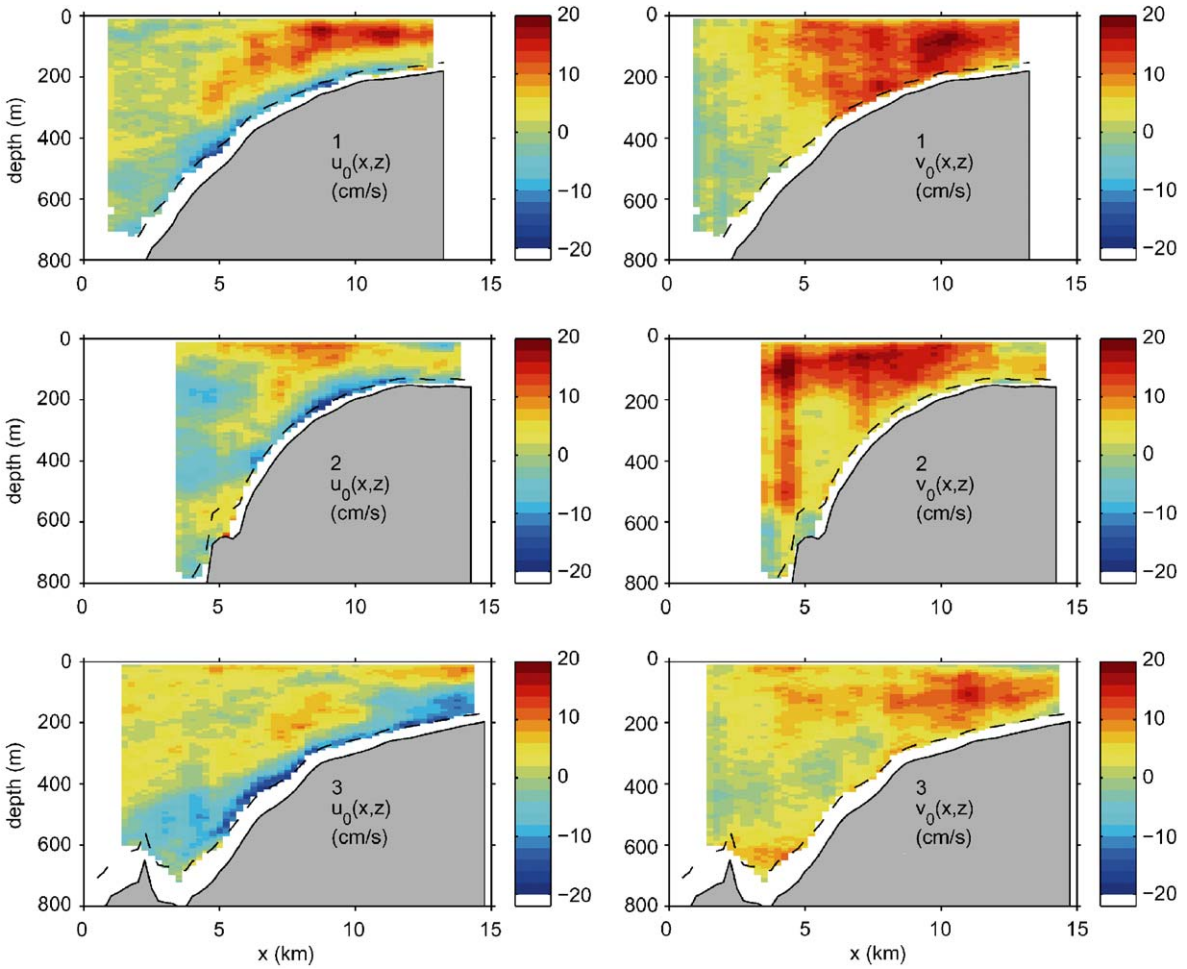

Fig. 11. Estimated total stationary currents cross-slope (left) and along-slope (right) in cm/s for transect 1 (top), transect 2 (middle) and transect 3 (bottom). Dashed lines represent 85% of the waterdepth, as in Fig. 7.

subsurface jet. The jet axis is at some 100 m depth and its width is similar to that of the barotropic part. Similar observations were made in this area by Pingree and Le Cann (1989), Pérenne (1997) and Pérenne and Pichon (1999). In models of tidal rectification (Maas and Zimmerman 1989b; Chen and Beardsley, 1995; Zhang et al., 1996) the along-isobath jet is surface-trapped in near-homogeneous conditions as the tidally rectified flow is impeded by friction close to the bottom. In principle this predicts its surface intensification. However, stratification inhibits the stretching and squeezing of vortex tubes further away from the bottom, limiting the rectification process to the near-bottom region. As a consequence, tidally rectified along-isobath flow in a stratified sea develops a subsurface maximum, as observed. Near the shelf break, and further on the shelf, drifter observations (a Lagrangian measurement) support this Eulerian current pattern (Mazé, 1987), and show that it is not annihilated by the Stokes' drift. In the cross-isobath direction, however, New (1988) finds in a numerical model an *upslope* Stokes' drift which *does* annihilate the strong near-bottom Eulerian downslope current, so as to satisfy the requirement (Wunsch, 1971) of zero net Lagrangian cross-isobath, isopycnal displacements.

The down-slope cross-isobath currents become up-slope from about a quarter of the water-column upwards. Further down the slope some near-bottom up-slope motion is observed. The cross-isobath currents seem to form part of a strong circulation cell (not very clearly visible along transect 3) that suggest an off-shelf upwelling area, near $x = 4$ km, over water-depths of some 500–600 m, and a downwelling higher up on the slope, beyond our most shallow, on-shelf measurement location. This suggestion is based on predictions from analytical and numerical models concerned with the cross-isobath structure of the cross-isobath, tidally rectified residual circulation (Maas and Zimmerman, 1989b, Chen and Beardsley, 1995).

5. Summary and discussion

Elementary theory, supported by the results of earlier laboratory experiments, indicate that in a continuously stratified fluid internal waves propagate their energy obliquely through the fluid in beams, parallel to their phase lines. While this kind of propagation has previously been observed in the ocean, such observations were traditionally based on comparing velocity records of some isolated moored instruments with predictions from a 2D numerical model. Here, we employed an alternative observational method that directly visualized the oceanic internal tidal beam emanating from the shelf edge of the Bay of Biscay. Comparison with the numerically predicted internal-tide field shows good correspondence even in details of the current fields. Moreover, the observational method concurrently reveals spatial details of the barotropic tide and of the residual flow in the vicinity of the shelf edge.

The observed barotropic tide had a tendency to conserve its cross-isobath mass flux (as presupposed in many theoretical studies). While there was correspondence in the amplitude estimates, the phase of the barotropic tide varied rapidly over the three cross-isobath transects. To some extent this can be attributed to the fact that our estimates resolve only one semi-diurnal tide constituent, representing M_2. Contributions from other nearby frequencies, such as S_2, N_2 which are present in the region, result in a larger phase change in the analysed (mixed) signal. But, this is insufficient to provide a full explanation. While we remain puzzled as to its immediate cause we speculate that it may reflect the barotropic tidal response to small-scale bathymetric features like canyons (Codiga et al., 1999).

The observed baroclinic tidal field showed phase lines (and corresponding amplitude lines) slanting downwards into the deep sea, under an angle that corresponds with that of the numerical model. A nodal point (amphidrome) in the vertical plane and the complex amplitude distribution find their counterparts in pictures computed with a linear 2D hydrostatic model. These patterns to a large extent reflect 'complexities' in stratification and bathymetry: the deeper, continuous stratification, corresponding to the permanent thermocline, is capped by a stronger seasonal thermocline, while the bottom sometimes also shows sharp corners or bumps. This leads to the barotropic forcing term

having multiple peaks over the vertical transect, one peak in the seasonal and one in the permanent thermocline, with further 'structure' due to bathymetric features. However, it was also shown that the forcing term, taken in isolation, does not necessarily indicate where the actual forcing is strongest; also important is the alignment of the barotropic current field with respect to the direction of internal-tide propagation, a fact that singles out near-critical slope regions as the dominant ones.

The slanting of phase lines is consistent with energy propagation into the deeper parts of the Bay of Biscay. While the present observations only reveal its initial generation and descent, this picture ties in with that sketched on the basis of previous observations from moorings that reveal the subsequent bottom reflection of this beam, upward propagation, and reflection from the seasonal thermocline, approximately 140 km away from the shelf edge (New and Pingree, 1992). Gerkema (2001) shows that this beam can under certain conditions on the stratification lead to the local generation of large amplitude internal waves in this seasonal thermocline, consistent with observations in New and Pingree (1992) and New and Da Silva (2002). This means that the beam is weakened and becomes less recognizable. One may speculate that internal tides may also originate from the opposite site, the Iberian shelf, and then be amplified upon reflection at the slope. Indirect evidence of such a reflection is described by Gemmrich and van Haren (2001).

The structure of the observed residual current is fairly consistent with that of a tidally rectified current. It reveals both an along-isobath current having its shallow side at its right-hand side (facing downstream) and a cross-isobath circulation dominated by down-slope flow just outside the bottom boundary layer (with a concurrent up-slope flow closer to the surface). Over the deeper parts of the slope this downslope bottom flow meets with an upslope bottom flow. The confluence leads to upwelling and may also be responsible for the 'cold ribbon' that is often encountered over the shelf edge.

While sunglint observations (Pingree and New, 1995) suggest the shelf to act as a 2D line source, one should realize that these surface manifestations reflect the properties of the internal tides only so far as they manifest themselves near the thermocline; the deeper (abyssal) internal tidal beams may have a different character. Three-dimensionality may be expected because the shelf edge is after all filled with submarine canyons, some of which may be particularly effective in internal tide generation. Petruncio et al. (1998) reported detailed measurements of the internal tide in a specific submarine canyon on the Pacific coast, together with numerical investigations (Petruncio, 1996). Ring-like structures suggest that such 'point-wise' generated internal tides also exist in the Bay of Biscay (Pingree et al., 1983; New, 1988), and their phase propagation was observed at sea (Holt and Thorpe, 1997) and in numerical models (Serpette and Mazé, 1989). In our own measurements this may be evident in 'anomolous' waves near a local seamount, along Section 3 (at $x = 2$ km), which were repeatedly encountered and gave rise to strong local current variations. It may well be that individual scatterers are also effective locally in converting barotropic to baroclinic tides, and are underestimated in 2D theory.

Acknowledgements

We are greatly indebted to H.M. van Aken, who designed the field program, to S. Ober and C. Veth for their assistance with the ADCP observations, to captain and crew of RV *Pelagia* and to P. Berkhout who first analyzed the data in his master thesis (IMAU V-97-15, Utrecht University). Finally, we are grateful to three referees whose suggestions helped us to improve the manuscript.

References

Baines, P.G., 1973. The generation of internal tides by flat-bump topography. Deep-Sea Research 20, 179–205.

Baines, P.G., 1982. On internal tide generation models. Deep-Sea Research 29, 307–388.

Blaas, M., 2002. Continental slope currents and shelf-sea circulation; dynamic effects of density forcing and tides. Ph.D. Thesis, Utrecht University.

Blaas, M., Lam, F.-P.A., Gerkema, T., de Swart, H.E., 2000. On slope currents forced by density gradients and tidal rectification. In: Yanagi, T. (Ed.), Interactions between Estuaries, Coastal Seas and Shelf Seas, Terra Scientific Publ. Comp., Tokyo, pp. 233–250.

Butman, B., Beardsley, R.C., Magnell, B., Frye, D., Vermersch, J.A., Schiltz, R., Limeburner, R., Wright, W.R., Noble, M.A., 1982. Recent observations on the mean circulation on Georges Bank. Journal of Physical Oceanography 12, 569–591.

Candela, J., Beardsley, R.C., Limeburner, R., 1992. Separation of tidal and subtidal currents in ship-mounted acoustic Doppler current profiler observations. Journal of Geophysical Research 97 (C1), 769–788.

Cartwright, D.E., Edden, A.C., Spencer, R., Vassie, J.M., 1980. The tides of the northeast Atlantic Ocean. Philosophical Transactions of the Royal Society of London A 298, 87–139.

Chen, C., Beardsley, R.C., 1995. A numerical study of stratified tidal rectification over finite-amplitude banks. Part I: symmetric banks. Journal of Physical Oceanography 25 (9), 2090–2110.

Codiga, D.L., Renouard, D.P., Fincham, A.M., 1999. Experiments on waves trapped over the continental slope and shelf in a continuously stratified rotating ocean, and their incidence on a canyon. Journal of Marine Research 57 (4), 585–612.

Dalziel, S.B., Hughes, G.O., Sutherland, B.R., 1998. Synthetic schlieren. Proceedings of the 8th International Symposium on Flow Visualization.

deWitt, L.M., Levine, M.D., Paulson, C.A., Burt, W.V., 1986. Semidiurnal internal tide in JASIN: observations and simulation. Journal of Geophysical Research 91 (C2), 2581–2592.

Eriksen, C.C., 1991. Observations of amplified flows atop a large seamount. Journal of Geophysical Research 96, 15227–15236.

Garrett, C.J.R., Loder, J.W., 1981. Dynamical aspects of shallow sea fronts. Philosophical Transactions of the Royal Society of London A 302, 563–581.

Gemmrich, J.R., van Haren, H., 2001. Thermal fronts generated by internal waves propagating obliquely along the continental slope. Journal of Physical Oceanography 31 (3), 649–655.

Gerkema, T., 2001. Internal and interfacial tides: beam scattering and local generation of solitary waves. Journal of Marine Research 59, 227–255.

Gerkema, T., 2002. Application of an internal-tide generation model to baroclinic spring-neap cycles. Journal of Geophysical Research 107 (C9), 3124 doi:10.1029/2001JC001177.

Gerkema, T., Lam, F.-P.A., Maas, L.R.M., in press. Internal tides in the Bay of Biscay: conversion rates and seasonal effects. Deep-Sea Research II.

Geyer, W.R., Signell, R., 1990. Measurements of tidal flow around a headland with a shipboard acoustic Doppler current profiler. Journal of Geophysical Research 95 (C3), 3189–3197.

Görtler, H., 1943. Über eine Swingungserscheinung in Flüssigkeiten mit stabiler Dichteschichtung. Zeitschrift fuer Angewandte Mathematik und Mechanik 23, 65–71.

Grimshaw, R.H.J., Baines, P.G., Bell, R.C., 1985. The reflection and diffraction of internal waves from the junction of a slit and a half-space, with applications to submarine canyons. Dynamics of Atmosphere and Oceans 9 (2), 85–120.

Holt, J.T., Thorpe, S.A., 1997. The propagation of high frequency internal waves in the Celtic Sea. Deep-Sea Research I 44 (12), 2087–2116.

Howarth, M.J., Huthnance, J.M., 1984. Tidal and residual currents around a Norfolk Sandbank. Estonian Coastal Shelf Science 19, 105–117.

Huthnance, J.M., 1973. Tidal current asymmetries over the Norfolk Sandbanks. Estuarine Coastal Marine Science 1, 89–99.

Huthnance, J.M., 1984. Slope currents and JEBAR. Journal of Physical Oceanography 14 (4), 795–810.

Huthnance, J.M., 1992. Extensive slope currents and the ocean-shelf boundary. Progress in Oceanography 29, 161–196.

Kazantsev, E., Sommeria, J., Verron, J., 1998. Subgrid-scale eddy parametrization by statistical mechanics in a barotropic ocean model. Journal of Physical Oceanography 28, 1017–1042.

Kunze, E., Toole, T.M., 1997. Tidally driven vorticity, diurnal shear, and turbulence atop Fieberling Seamount. Journal of Physical Oceanography 27, 2663–2693.

Le Cann, B., 1990. Barotropic tidal dynamics of the Bay of Biscay shelf: observations, numerical modelling and physical interpretation. Continental Shelf Research 10 (8), 723–758.

LeBlond, P.H., Mysak, L.A., 1978. Waves in the Ocean. Elsevier Oceanography Series. Elsevier, Amsterdam.

Leont'yeva, Y.A., Sabinin, K.D., Shulepov, V.A., Yampol'skiy, A.D., 1992. Experimental data on internal tides at the Mascarene Ridge and their ray tracing. Oceanology 32 (6), 707–712.

Loder, J.W., Wright, D.G., 1985. Tidal rectification and frontal circulation on the sides of Georges Bank. Journal of Marine Research 43, 581–604.

Loder, J.W., Brickman, D., Horne, E.P.W., 1992. Detailed structure of currents and hydrography on the northern side of Georges Bank. Journal of Geophysical Research 97 (C9), 14331–14351.

Lwiza, K.M.M., Bowers, D.G., Simpson, J.H., 1991. Residual and tidal flow at a tidal mixing front in the North Sea. Continental Shelf Research 11 (11), 1379–1395.

Maas, L.R.M., Lam, F.-P.A., 1995. Geometric focusing of internal waves. Journal of Fluid Mechanics 300, 1–41.

Maas, L.R.M., van Haren, J.J.M., 1987. Observations on the vertical structure of tidal and inertial currents in the central North Sea. Journal of Marine Research 45, 293–318.

Maas, L.R.M., Zimmerman, J.T.F., 1989a. Tide-topography interactions in a stratified shelf sea I. Basic equations for quasi-nonlinear internal tides. Geophysical and Astrophysical Fluid Dynamics 45, 1–35.

Maas, L.R.M., Zimmerman, J.T.F., 1989b. Tide-topography interactions in a stratified shelf sea II. Bottom trapped internal tides and baroclinic residual currents. Geophysical and Astrophysical Fluid Dynamics 45, 37–69.

Maas, L.R.M., Benielli, D., Sommeria, J., Lam, F.P.A., 1997. Observation of an internal wave attractor in a confined, stably stratified fluid. Nature 388, 557–561.

Mazé, R., 1987. Generation and propagation of non-linear internal waves induced by the tide over a continental slope. Continental Shelf Research 7, 1079–1104.

Miles, J.W., 1972. Kelvin waves on oceanic boundaries. Journal of Fluid Mechanics 55, 113–127.

Morozov, E.G., 1995. Semidiurnal internal wave global field. Deep-Sea Research I 42 (1), 135–148.

Mowbray, D.E., Rarity, B.S.H., 1967. A theoretical and experimental investigation of the phase configuration of internal waves of small amplitude in a density stratified liquid. Journal of Fluid Mechanics 28, 1–16.

New, A.L., 1988. Internal tidal mixing in the Bay of Biscay. Deep-Sea Research 35 (5), 691–709.

New, A.L., Da Silva, J.C.B., 2002. Remote-sensing evidence for the local generation of internal soliton packets in the central Bay of Biscay. Deep-Sea Research I 49, 915–934.

New, A.L., Pingree, R.D., 1992. Local generation of internal soliton packets in the central Bay of Biscay. Deep-Sea Research 39 (9), 1521–1534.

Ou, H.W., 1999. A model of tidal rectification by potential vorticity mixing. Part I: homogeneous ocean. Journal of Physical Oceanography 29, 821–827.

Ou, H.W., Maas, L.R.M., 1986. Tidal-induced buoyancy flux and mean transverse circulation. Continental Shelf Research 5 (6), 611–628.

Pérenne, N., 1997. Etude expérimentale et numérique de la rectification topographique en milieu homogène ou stratifié. Ph.D. Thesis, University of Joseph Fourier-Grenoble 1, Grenoble, France.

Pérenne, N., Pichon, A., 1999. Effect of barotropic tidal rectification on low-frequency circulation near the shelf break in the northern Bay of Biscay. Journal of Geophysical Research 104 (C6), 13489–13506.

Petruncio, E.T., 1996. Observations and modeling of the internal tide in a submarine canyon. Ph.D. Thesis, Naval Postgraduate School, Monterey, CA.

Petruncio, E.T., Rosenfeld, L.K., Paduan, J.D., 1998. Observations of the internal tide in Monterey Canyon. Journal of Physical Oceanography 28 (10), 1873–1903.

Pichon, A., Mazé, R., 1990. Internal tides over a shelf break: analytical model and observations. Journal of Physical Oceanography 20 (5), 657–671.

Pingree, R.D., 1979. Baroclinic eddies bordering the Celtic Sea in late summer. Journal of Marine Biological Association UK 59, 689–698.

Pingree, R.D., 1984. Some applications of remote sensing to studies in the Bay of Biscay, Celtic Sea and English Channel. Elsevier Oceanographic Series 38, 287–315.

Pingree, R.D., Le Cann, B., 1989. Celtic and Armorican slope and shelf residual currents. Progress in Oceanography 23, 303–338.

Pingree, R.D., Le Cann, B., 1990. Structure, strength and seasonality of the slope currents in the Bay of Biscay region. Journal of Marine Biological Association UK 70, 857–885.

Pingree, R.D., Mardell, G.T., 1985. Solitary internal waves in the Celtic Sea. Progress in Oceanography 14, 413–441.

Pingree, R.D., New, A.L., 1989. Downward propagation of internal tidal energy into the Bay of Biscay. Deep-Sea Research 36 (5), 735–758.

Pingree, R.D., New, A.L., 1991. Abyssal penetration and bottom reflection of internal tidal energy into the Bay of Biscay. Journal of Physical Oceanography 21 (1), 28–39.

Pingree, R.D., New, A.L., 1995. Structure, seasonal development and sunglint spatial coherence of the internal tide on the Celtic and Armorican shelves and in the Bay of Biscay. Deep-Sea Research I 42 (2), 245–284.

Pingree, R.D., Griffiths, D.K., Mardell, G.T., 1983. The structure of the internal tide at the Celtic Sea shelf break. Journal of Marine Biological Association UK 64, 99–113.

Pingree, R.D., Mardell, G.T., New, A.L., 1986. Propagation of internal tides from the upper slopes of the Bay of Biscay. Nature 321, 154–158.

Prandle, D., 1982. The vertical structure of tidal currents and other oscillatory flows. Continental Shelf Research 1, 191–207.

Ray, R.D., Mitchum, G.T., 1997. Surface manifestation of internal tides in the deep ocean: observations from altimetry and island gauges. Progress in Oceanography 40, 135–162.

Serpette, A., Mazé, R., 1989. Internal tides in the Bay of Biscay: a two-dimensional model. Continental Shelf Research 9 (9), 795–821.

Sherwin, T.J., Taylor, N.K., 1990. Numerical investigations of linear internal tide generation in the Rockall Trough. Deep-Sea Research 37 (10), 1595–1618.

Simpson, J.H., Mitchelson-Jacob, E.G., Hill, A.E., 1990. Flow structure in a channel from an acoustic Doppler current profiler. Continental Shelf Research 10 (6), 589–603.

Smith, W.H.F., Sandwell, D.T., 1997. Global sea floor topography from satellite altimetry and ship depth soundings. Science 277 (5334), 1956–1962.

Sutherland, B.R., Dalziel, S.B., Hughes, G.O., Linden, P.F., 1999. Visualisation and measurement of internal waves by synthetic schlieren. Part 1: vertically oscillating cylinder. Journal of Fluid Mechanics 390, 93–126.

Sutherland, B.R., Hughes, G.O., Dalziel, S.B., Linden, P.F., 2000. Internal waves revisited. Dynamics of Atmosphere and Oceans 31, 209–232.

Tee, K.T., 1985. Depth-dependent studies of tidally induced residual currents on the sides of Georges Bank. Journal of Physical Oceanography 15, 1818–1846.

Thorpe, S.A., 1999. The generation of alongslope currents by breaking internal waves. Journal of Physical Oceanography 29, 29–38.

van Aken, H.M., 2000. The hydrography of the mid-latitude Northeast Atlantic Ocean; II: the intermediate water masses. Deep-Sea Research I 47, 789–824.

van Haren, J.J.M., Maas, L.R.M., 1987. Temperature and current fluctuations due to tidal advection of a front. Netherlands Journal of Sea Research 21, 79–94.

Vlasenko, V.I., Morozov, Y.G., 1993. Generation of semidiurnal internal waves near a submarine ridge. Oceanology 33 (3), 282–286.

Wright, D.G., Loder, J.W., 1985. A depth-dependent study of topographic rectification of tidal currents. Geophysical and Astrophysical Fluid Dynamics 31, 169–220.

Wunsch, C., 1971. Note on some Reynolds stress effects of internal waves on slopes. Deep-Sea Research 18, 583–591.

Zhang, X., Boyer, D.L., Pérenne, N., Renouard, D.P., 1996. Mean flow generation along a sloping region in a rotating homogeneous fluid. Journal of Geophysical Research 101 (C12), 28597–28614.

Zimmerman, J.T.F., 1978. Topographic generation of residual circulation by oscillatory (tidal) currents. Geophysical and Astrophysical Fluid Dynamics 11, 35–47.